

Coherent elastic neutrino-nucleus scattering with the ν BDX-DRIFT directional detector at next generation neutrino facilities

D. Aristizabal Sierra,^{1,2,*} Bhaskar Dutta,^{3,†} Doojin Kim,^{3,‡} Daniel Snowden-Ifft,^{4,§} and Louis E. Strigari^{3,¶}

¹*Universidad Técnica Federico Santa María - Departamento de Física
Casilla 110-V, Avda. España 1680, Valparaíso, Chile*

²*IFPA, Dep. AGO, Université de Liège, Bat B5, Sart Tilman B-4000 Liège 1, Belgium*

³*Department of Physics and Astronomy, Mitchell Institute for Fundamental Physics and Astronomy,
Texas A&M University, College Station, TX 77843, USA*

⁴*Occidental College, Dept. of Physics, 1600 Campus Road, Los Angeles, CA, United States*

We discuss various aspects of a neutrino physics program that can be carried out with the neutrino Beam-Dump eXperiment DRIFT (ν BDX-DRIFT) detector using neutrino beams produced in next generation neutrino facilities. ν BDX-DRIFT is a directional low-pressure TPC detector suitable for measurements of coherent elastic neutrino-nucleus scattering (CEvNS) using a variety of gaseous target materials which include carbon disulfide, carbon tetrafluoride and tetraethyllead, among others. The neutrino physics program includes standard model (SM) measurements and beyond the standard model (BSM) physics searches. Focusing on the Long Baseline Neutrino Facility (LBNF) beamline at Fermilab, we first discuss basic features of the detector and estimate backgrounds, including beam-induced neutron backgrounds. We then quantify the CEvNS signal in the different target materials and study the sensitivity of ν BDX-DRIFT to measurements of the weak mixing angle and neutron density distributions. We consider as well prospects for new physics searches, in particular sensitivities to effective neutrino non-standard interactions.

I. INTRODUCTION

Coherent elastic neutrino-nucleus scattering (CEvNS) is a process in which neutrinos scatter on a nucleus which acts as a single particle. Within the Standard Model (SM), CEvNS is fundamentally described by the neutral current interaction of neutrinos and quarks, and due to the nature of SM couplings it is approximately proportional to the neutron number squared [1]. Following years of experimental efforts, the COHERENT collaboration has established the first detection of CEvNS using a stopped-pion source with both a CsI[Na] scintillating crystal detector [2] and single-phase liquid argon target [3].

There are many proposed experimental ideas to follow up on the detection of CEvNS, using for example reactor [4–11], SNS [12, 13], and ⁵¹Cr sources [14]. The COHERENT data and these future detections provide an exciting new method to study beyond the SM (BSM) physics through the neutrino sector, as well as provide a new probe of nuclear properties.

Since the power of CEvNS as a new physics probe is just now being realized, it is important to identify new ways to exploit CEvNS in future experiments. In this paper, we propose a new idea to study CEvNS with the neutrino Beam-Dump eXperiment Directional Identification From Tracks (ν BDX-DRIFT) detector using neutrino beams at next generation neutrino experiments. For concreteness we focus on the Long

Baseline Neutrino Facility (LBNF) beamline at Fermilab [15]. As we show, this experimental setup is unique relative to ongoing CEvNS experiments, for two primary reasons. First, the LBNF beam neutrinos are produced at a characteristic energy scale different than neutrinos from reactor or SNS sources. This provides an important new, third energy scale at which the CEvNS cross section can be studied. Second, our detector has directional sensitivity, which improves background discrimination and signal extraction. Previous studies have shown how directional sensitivity improves sensitivity for BSM searches [16].

This paper is organized as follows. In Section II we discuss the basic features of the ν BDX-DRIFT detector setup that we are considering. In Section III we discuss the expected CEvNS signal at ν BDX-DRIFT. In Section IVA, we investigate the backgrounds at ν BDX-DRIFT and in Section IVB, we show the aspects of SM and BSM physics that can be studied using ν BDX-DRIFT. In Section V we present our conclusions.

II. ν BDX-DRIFT: BASIC DETECTOR FEATURES

As discussed in [17], a BDX-DRIFT detector, with its novel directional and background rejection capabilities, is ideally suited to search for elastic, coherent, low-energy, nuclear-recoils from light dark matter (DM). A sketch of a BDX-DRIFT detector is shown in Figure 1. The readouts on either end couple to two back-to-back drift volumes filled with a nominal mixture of 40 Torr CS₂ and 1 Torr O₂ and placed into a neutrino beam, as shown. The use of the electronegative gas CS₂ allows for the ionization to be transported through the gas with only thermal diffusion which largely preserves the shape

* daristizabal@ulg.ac.be

† dutta@physics.tamu.edu

‡ doojin.kim@tamu.edu

§ iff@oxy.edu

¶ strigari@tamu.edu

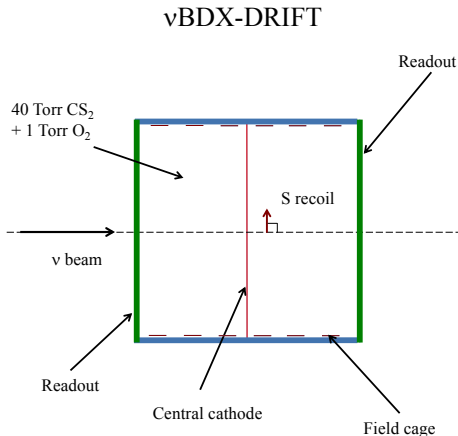


FIG. 1. A sketch of the vBDX-DRIFT detector.

of the track [18]. CS_2 releases the electron near the gain element allowing for normal electron avalanche to occur at the readout [18]. The addition of O_2 to the gas mixture allows for the distance between the recoil and the detector to be measured without a t_0 (time of creation of the ionization) [19–21] eliminating, with side-vetoes, prodigious backgrounds from the edges of the fiducial volume. Because of the prevalence of S in the gas and the Z^2 dependence for coherent, elastic, low-energy scattering, [17] the recoils would be predominantly S nuclei. With a threshold of 20 keV the S recoils would be scattered within one degree of perpendicular to the beam line due to extremely low-momentum transfer, scattering kinematics. The signature of these interactions, therefore, would be a population of events with ionization parallel to the detector readout planes.

Here we consider deploying a BDX-DRIFT detector in a neutrino beam of a next generation neutrino facility, which for definitiveness we take to be the LBNF beamline at Fermilab. As discussed below CEvNS will produce low-energy nuclear recoils in the fiducial volume of a vBDX-DRIFT detector. To optimize the detector for CEvNS detection various gas mixtures and pressures are considered.

III. CEvNS IN vBDX-DRIFT

When the neutrino-nucleus exchanged momentum is small enough ($q \lesssim 200 \text{ MeV}$) the individual nucleon amplitudes sum up coherently, resulting in a coherent enhancement of the neutrino-nucleus cross section [1]. So rather than scattering off nucleons the neutrino scatters off the entire nucleus. This constraint on q translates into an upper limit on the neutrino energy $E_\nu \lesssim 100 \text{ MeV}$, which in turn “selects” the neutrino sources capable of inducing CEvNS. At the laboratory level, reactor neutrinos with $E_\nu \lesssim 9 \text{ MeV}$ dominate the low energy window, while stopped-pion sources with $E_\nu < m_\mu/2$ the in-

termediate energy window. Fig. 2 shows the different energy domains at which CEvNS can be induced. At the astrophysical level CEvNS can be instead induced by solar, supernova and atmospheric neutrinos in the low, intermediate and “high” energy windows, respectively.

Using laboratory-based sources, CEvNS has been measured by the COHERENT collaboration with CsI[Na] and LAr detectors [2, 22]. And measurements using reactor neutrino sources are expected in the near-future [6, 8, 23]. The high-energy window however has been rarely discussed and experiments covering that window have been so far not considered. One of the reasons is probably related with the conditions that should be minimally satisfied for an experiment to cover that energy range: (i) The low-energy tail of the neutrino spectrum should provide a sufficiently large neutrino flux, (ii) the detector should be sensitive to small energy depositions and (iii) backgrounds need to be sufficiently small to observe the signal. The LBNF beamline combined with the vBDX-DRIFT detector satisfy these three criteria, as we will now demonstrate.

Accounting for the neutron and proton distributions independently, i.e. assuming that their root-mean-square (rms) radii are different $\langle r_n^2 \rangle \neq \langle r_p^2 \rangle$, the SM CEvNS differential cross section reads [1, 24]

$$\frac{d\sigma}{dE_r} = \frac{m_N G_F^2}{2\pi} \left(2 - \frac{E_r m_N}{E_\nu^2} \right) Q_W^2, \quad (1)$$

where the coherent weak charge quantifies the Z -nucleus vector coupling, namely

$$Q_W^2 = [N g_V^n F_N(q) + Z g_V^p F_Z(q)]^2. \quad (2)$$

The proton and neutron charges are determined by the up and down quark weak charges and read $g_V^n = -1/2$ and $g_V^p = 1/2 - 2 \sin^2 \theta_W$. In the Born approximation the nuclear form factors are obtained from the Fourier transform of the neutron and proton density distributions. The properties of these distributions are captured by different parametrizations, which define different form factors. For all our calculations we use the one provided by the Helm model [25], apart from Section IV B 2 where we will as well consider those given by the symmetrized Fermi distribution function and the Klein-Nystrand approach [26, 27] (see that Section for details). Note that the dependence that the signal has on the form factor choice is a source for the signal uncertainty.

In almost all analyses $\langle r_n^2 \rangle = \langle r_p^2 \rangle$, and so the form factor factorizes. That approximation is good enough unless one is concerned about percent effects [28, 29], $\langle r_p^2 \rangle$ values for Z up to 96 are known at the part per thousand level through elastic electron-nucleus scattering [30]. In that limit one can readily see that the differential cross section is enhanced by the number of neutrons (N^2) of the target material involved, a manifestation of the coherent sum of the individual nucleon amplitudes. In what follows all our analyses will be done in that limit, the exception being Sec. IV B 2.

The differential event rate (events/year/keV) follows from a convolution of the CEvNS differential cross section and the

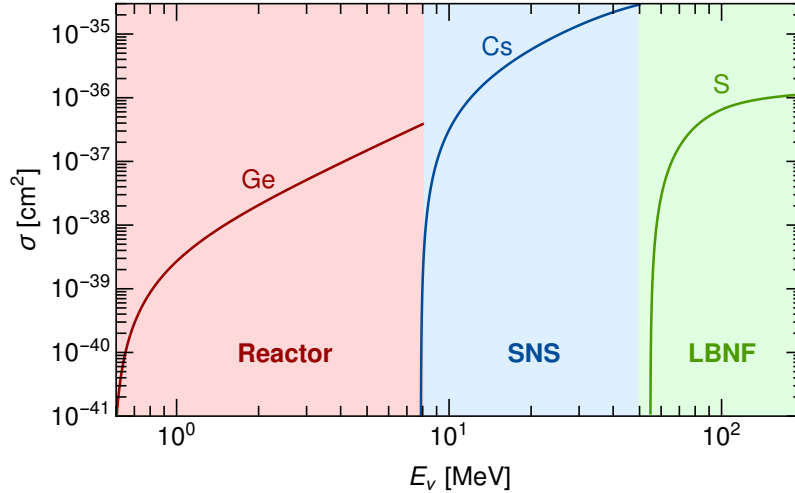


FIG. 2. CEvNS total cross section as a function of incoming neutrino energy for reactor neutrinos, spallation neutron source (SNS) neutrinos and the LBNF beamline. Cross sections are calculated for representative nuclides of the technologies used in each case: germanium (reactor), cesium (SNS) and sulfur (LBNF). This graph shows the different energy domains at which a significant CEvNS signal can be induced.

neutrino spectral function properly normalized

$$\frac{dR}{dE_r} = V_{\text{det}} \rho(P) \frac{N_A}{m_{\text{molar}}} \int_{E_r^{\text{min}}}^{E_r^{\text{max}}} \frac{d\sigma}{dE_r} \frac{d\Phi}{dE_\nu} dE_\nu. \quad (3)$$

Here $E_r^{\text{min}} = \sqrt{m_N E_r}/2$. The first two factors define the detector mass $m_{\text{det}} = V_{\text{det}} \rho(P)$, where $\rho(P)$ corresponds to the target material density which depends on detector pressure at fixed room temperature, $T = 293$ K. Assuming an ideal gas it reads,

$$\rho = 5.5 \times 10^{-5} \times \left(\frac{m_{\text{molar}}}{\text{g/mol}} \right) \left(\frac{P}{\text{Torr}} \right) \frac{\text{kg}}{\text{m}^3}. \quad (4)$$

Pressure and recoil energy threshold are related and their dependence varies with target material. For the isotopes considered here, assuming CS_2 to be the dominant gas, we have:

$$E_r^{\text{th}}(\text{Nuc}_i) = f_i \left(\frac{P}{40 \text{ Torr}} \right) \text{keV}, \quad (5)$$

with $f_i = \{2, 7.5, 13, 20, 69\}$ for $\text{Nuc}_i = \{\text{H}, \text{C}, \text{F}, \text{S}, \text{Pb}\}$ [19, 31]. For the neutrino spectrum (and normalization) we use the DUNE near detector flux prediction for three different positions (on-axis and off-axis 9 m (0.5° off-axis) and 33 m (2.0° off-axis)) [32]. Fig. 3 shows the corresponding fluxes (left graph) along with the low energy region relevant for CEvNS (right graph).

With these results we are now in a position to calculate the CEvNS event yield for potential different target materials (compounds): carbon disulfide, carbon tetrafluoride and tetraethyllead as a function of pressure (threshold). We start with carbon disulfide and assume the following detector configuration/operation values: $V_{\text{det}} = 10 \text{ m}^3$ and seven-year data taking. Results for smaller/larger detector volumes as well as for smaller/larger operation times follow from an overall scaling of the results presented here, provided the assumption of a pointlike detector is kept.

Left graph in Fig. 4 shows the CEvNS event rate for CS_2 , carbon and sulfur independently displayed. The result is obtained by assuming the on-axis neutrino flux configuration. One can see that up to 700 Torr the event rate is dominated by the sulfur contribution, point at which carbon overtakes the event rate with a somewhat degraded contribution. The individual behavior of each contribution can be readily understood as follows. At low recoil energies the event rate is rather flat but pressure is low, thus the suppression of both contributions in that region is due to low pressure. As pressure increases, m_{det} increases, as do the carbon and sulfur event rates. There is a pressure, however, for which the processes start losing coherence and so the event rates start decreasing accordingly (variations in pressure translate into variations in recoil energy threshold according to Eq. (5)). For sulfur it happens at lower pressures than for carbon, as expected given that sulfur is a heavier nucleus. For CS_2 then it is clear that the optimal pressure is set at about 400 Torr (exactly at 411 Torr), a value that corresponds to $E_r^{\text{th}} \simeq 77.1$ keV for carbon and to $E_r^{\text{th}} = 205.5$ keV for sulfur, according to Eq. (5). In summary, at the optimum pressure and corresponding threshold, for CS_2 the number of CEvNS events for a 7-year 10 cubic-meter exposure is 367.

Although rather energetic, it is clear that the LBNF beamline can induce CEvNS and that the process can be measured, provided the detector is sensitive to low recoil energies. The details of how CEvNS proceeds are as follows. The low-energy tail of the neutrino spectrum (on-axis) extends down to energies of order 50 MeV or so, as can be seen in the right graph in Fig. 3. From that energy and up to those where coherence is lost, the neutrino flux will induce a sizable number of CEvNS events. Taking the recoil energy at which $F^2(E_r)$ decreases from 1 to 0.1 as the energy at which coherence is lost (above those energies the nuclear form factor decreases rapidly and enters a dip, regardless of the nuclei), E_ν can be

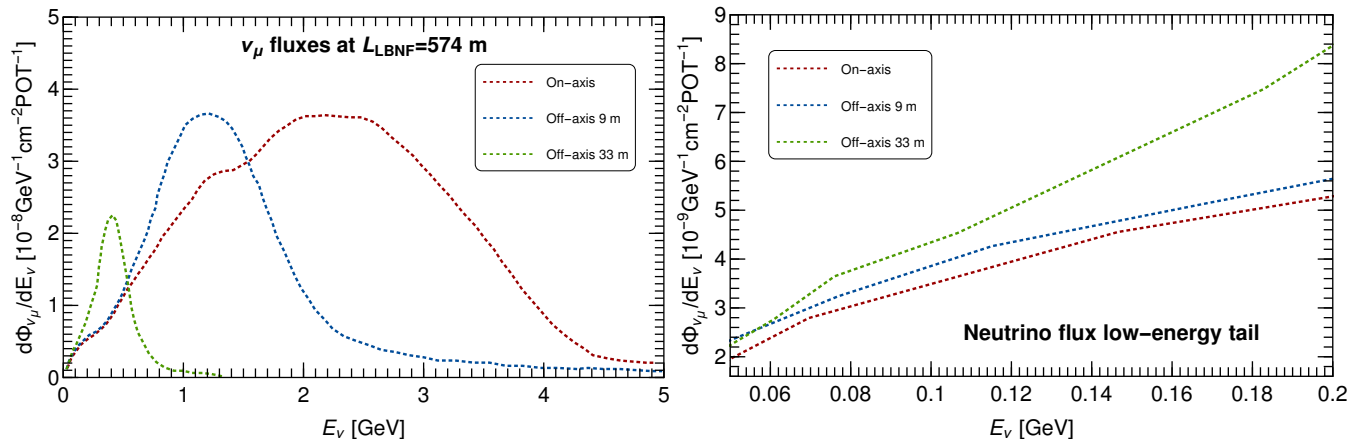


FIG. 3. **Left graph:** Neutrino flux at the vBDX-DRIFT location ($L_{\text{LBNF}} = 574$ m) for three positions: on-axis and off-axis 9 m and 33 m (0.5° and 2.0° off-axis) [32]. **Right graph:** Low-energy tail of the neutrino spectra, relevant for CEvNS, for the three positions considered in the left graph. See discussion in Section III for details.

determined with the aid of $E_\nu = \sqrt{2m_N E_r}$. Since for sulfur (carbon) we found $E_r^S \simeq 370$ keV ($E_r^C \simeq 1800$ keV), we get $E_\nu^S \simeq 150$ MeV ($E_\nu^C \simeq 200$ MeV). Numerically we have checked that the event yield changes only in one part per thousand when increasing E_r^{max} to values for which $E_\nu > 200$ MeV.

The number of muon neutrinos per year per cm^2 delivered by the LBNF beamline in the on-axis configuration and the full energy range, $[0.5, 5 \times 10^3]$ MeV, is 1.1×10^{14} . For the energy range that matters for CEvNS this number is instead 10^{12} . There are about two orders of magnitude less neutrinos for CEvNS than e.g. for elastic neutrino-electron scattering. However, the flux depletion is somewhat compensated by the N^2 enhancement of the CEvNS cross sections, which for sulfur (carbon) amounts to 256 (36). Thus, although fewer neutrinos are available for CEvNS, the large size of the corresponding cross section leads to a sizable number of events even for neutrino energies far above those of spallation neutron source neutrinos.

From Fig. 3, and as expected, it is clear that the number of neutrinos decreases as one moves off the axis. For the configurations shown there we calculate: and $n_\nu(33\text{m}) = 9.3 \times 10^{12} \nu_\mu/\text{year}/\text{cm}^2$ (integrating over the full neutrino energy range, $[5 \times 10^{-2}, 5]$ GeV). So the CEvNS event rates for these off-axis configurations are depleted, although as a function of pressure they keep the same behavior, as can be seen in the right graph in Fig. 4. Note that off-axis configurations, in particular that at 33 m, can potentially be ideal for light DM searches since they lead to a suppression of neutrino (or neutrino-related) backgrounds [33].

vBDX-DRIFT is suitable for other target materials as well, so we have investigated the behavior of their event rates. The left graph in Fig. 5 shows the result for carbon tetrafluoride (CF_4), while the right graph for tetraethyllead ($\text{C}_8\text{H}_{20}\text{Pb}$). For the results in the left graph we have assumed the bulk of the gas is filled with CF_4 , i.e. 100% of the fiducial volume is filled with CF_4 . Note that this is a rather good approximation given that CS_2 and CF_4 have about the same number of elec-

trons per molecule. For the results in the right graph we have instead taken a $\text{CS}_2:\text{C}_8\text{H}_{20}\text{Pb}$ concentration of 2.3:1. As we will discuss in Section IV B 2, these compounds are particularly useful for measurements of the root-mean-square (rms) radius of the neutron distributions of carbon, fluorine and lead.

From these results one can see that for carbon tetrafluoride the signal is dominated by fluorine, with subdominant contributions from carbon. Fluorine being a slightly heavier nuclei has intrinsically a larger cross section, with an enhancement factor of order $(N_F/N_C)^2 = 100/36 \simeq 2.8$. In addition the carbon-to-fluorine ratio of the compound implies an extra factor 4 for the fluorine contribution. One can see as well that up to 1200 Torr the signal increases. For analyses in CF_4 we take the CEvNS signal at 400 Torr, for which we get 808 events/7-years.

In terms of pressure, tetraethyllead behaves rather differently. The signal is dominated by lead up to 12 Torr or so. At that point the carbon contribution kicks in and dominates the signal, particularly at high pressure. Hydrogen contributes to the signal at the per mille level, despite being enhanced by a factor 20 from the molecular composition. This is expected, in contrast to the carbon and lead cross sections the hydrogen contribution is not enhanced. The behavior of the lead and carbon contributions can be readily understood. Relative to lead the carbon coherence enhancement factor is small $(N_C/N_{\text{Pb}})^2 \simeq 2.3 \times 10^{-3}$. However, lead loses coherence at rather low pressures and so the difference is mitigated. One can see that for $P < 12$ Torr carbon contributes at the percent level.

The pressure at which the lead signal peaks is relevant if one is interested in lead related quantities. That pressure corresponds to 6.4 Torr, for which carbon contributes about 25% of the total signal. At that pressure the signal amounts to 26 events/7-years, with the contribution from lead (carbon) equal to 19.2 events/7-years (6.7 events/7-years). Thus for such measurements one will need as well to distinguish recoils in lead from those in carbon, something that seems vi-

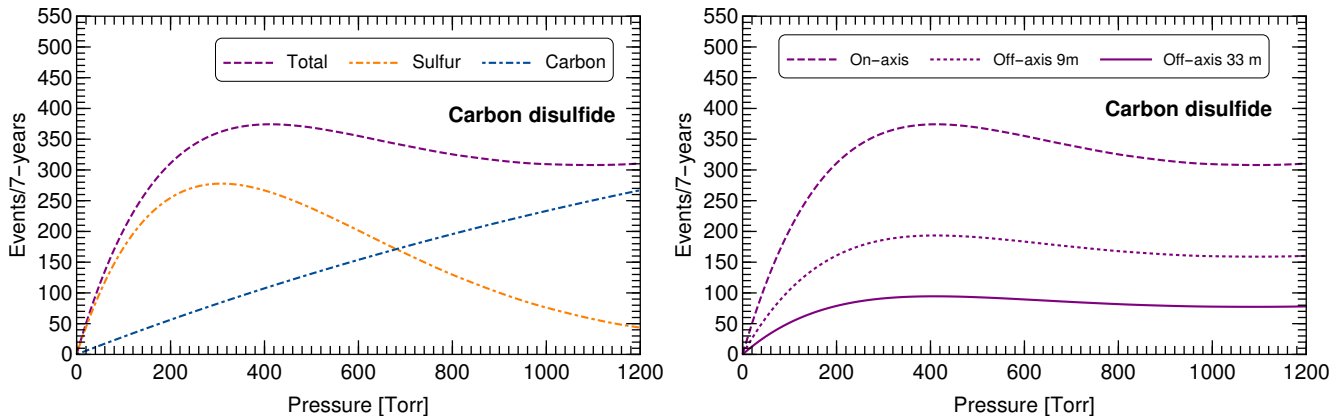


FIG. 4. **Left graph:** CEvNS event yield for carbon dioxide in terms of pressure assuming a ten-cubic meter detector volume operating at room temperature during a 7-years data taking period. **Right graph:** CEvNS event yield for different detector position configurations: on-axis and off-axis 9 m and 33 m (0.5° and 2.0° off-axis).

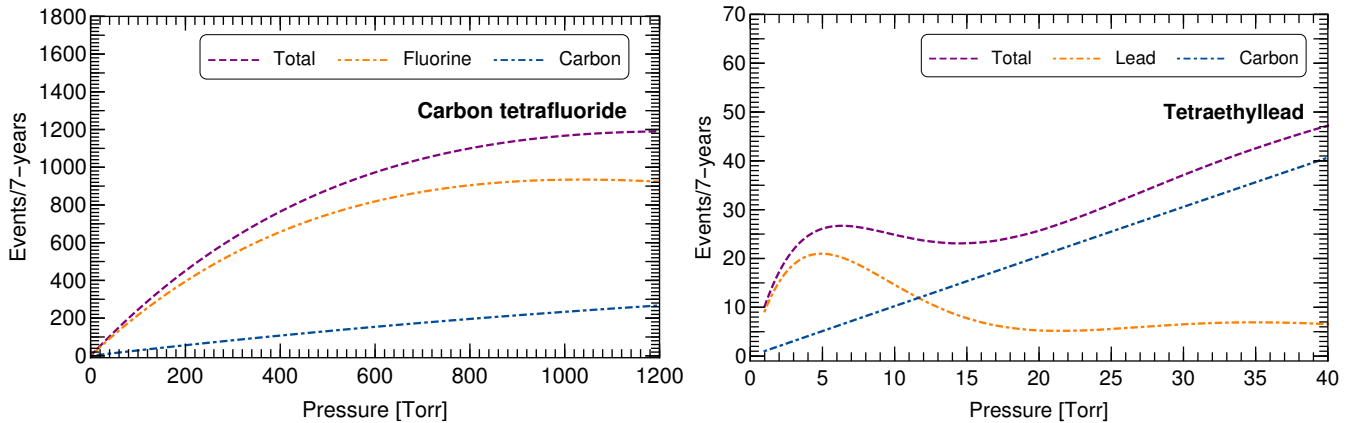


FIG. 5. **Left graph:** CEvNS event rates as a function of pressure for carbon tetrafluoride (CF_4) assuming a ten-cubic meter detector volume, operation at room temperature and on-axis neutrino flux configuration. The calculation assumes the bulk of the gas is filled with CF_4 . **Right graph:** Same as left graph but for tetraethyllead ($\text{C}_8\text{H}_{20}\text{Pb}$). Hydrogen contributes to the signal at the per mille level and so its contribution is not displayed. In contrast to CF_4 , in this case a concentration of 2.3:1 of carbon disulfide and tetraethyllead has been assumed.

able given that the range of C for a given ionization should be much larger than for Pb.

IV. $\nu\text{BDX-DRIFT}$ PHYSICS POTENTIAL BEYOND CEvNS MEASUREMENTS

After discussing CEvNS measurements with the $\nu\text{BDX-DRIFT}$ detector, we now proceed with a discussion of possible problematic backgrounds as well as studies that can be carried out with the detector. For the latter we split the discussion in measurements of SM quantities and BSM searches. We would like to stress that although BSM searches at $\nu\text{BDX-DRIFT}$ include those for light DM, here we limit our discussion to the case of new interactions in the neutrino sector that can potentially affect the CEvNS event spectrum. The discussion of light DM will be presented elsewhere [33].

A. Estimation of backgrounds at $\nu\text{BDX-DRIFT}$

DRIFT detectors have been shown to be insensitive to all types of ionizing radiation except nuclear recoils after analysis cuts have been applied with minimal loss of sensitivity [19]. The most recent results from the Boulby Mine show no nuclear recoil events in the fiducial volume in 55 days of running [19]. These results have been extended now to 150 days of running [34]. Furthermore DRIFT detectors have been run on the surface and only been found to be sensitive to cosmic ray neutrons [35]. The DUNE near detector site is at a depth of 60 m and any possibility of nuclear recoils induced from cosmic rays at this shallower depth than the Boulby Mine would be vetoed by timing cuts. The several second cycle time of the LBNF beam is ideally suited to the slow drift speed of a DRIFT detector. Thus beam-unrelated backgrounds will not be a limitation at LBNF.

Beam-related backgrounds are possibly concerning. In this

section we address the most worrisome beam-related background, neutrino-induced neutrons (NINs). The neutrino beam interacts not only with the target material but with the vessel walls as well. In that process, some neutrinos can interact with the nucleons of the vacuum vessel to produce neutrons, which could enter the active detector volume and produce a background of low-energy nuclear-recoils. Depending on the neutrino beam energy distribution, and the vacuum vessel material, different processes are to be considered. For an iron vessel (mostly ^{56}Fe) and $E_\nu \lesssim 0.1$ GeV, the incoming neutrino can strip off a neutron from ^{56}Fe , thus inducing the stripping reaction $^{56}\text{Fe} + \nu_\mu \rightarrow n + ^{55}\text{Fe} + \nu_\mu$. The total cross section for this processes ranges from 10^{-42} cm² to 10^{-41} cm², and dominates NIN production in that neutrino energy regime [36].

For neutrino energies above ~ 0.1 GeV other processes can dominate. The on-axis LBNF spectrum peaks within 2-3 GeV and extends up to energies of order 5 GeV (see Fig. 3). Thus, although LBNF neutrinos trigger iron stripping reactions, their rate is small compared to neutrino processes which open up as soon as $E_\nu \gtrsim 0.1$ GeV, namely: elastic scattering (E); quasielastic scattering (QE); resonant single pion production (RES); deep inelastic scattering (DIS).¹ Of course, not all these processes produce final state neutrons, only E and RES do. For initial-state neutrinos, RES processes are [37]

$$\text{CC: } \nu_\mu + p \rightarrow \mu^- + p + \pi^+, \quad \nu_\mu + n \rightarrow \mu^- + p + \pi^0, \\ \nu_\mu + n \rightarrow \mu^- + n + \pi^+, \quad (6)$$

$$\text{NC: } \nu_\mu + p \rightarrow \nu_\mu + p + \pi^0, \quad \nu_\mu + p \rightarrow \nu_\mu + n + \pi^+, \\ \nu_\mu + n \rightarrow \nu_\mu + n + \pi^0, \quad \nu_\mu + n \rightarrow \nu_\mu + p + \pi^-. \quad (7)$$

Thus, only three out of seven involve final-state neutrons which could give recoils mimicking the signal. As can be seen in Eq. (6) RES CC processes produce as well charged products which would likely be picked up in the fiducial volume and so vetoed, but are included here for a generous estimate of the backgrounds. The protons produced by the other processes could produce recoils but are charged and so could be similarly vetoed. Pions are either charged and so can be vetoed or uncharged and decaying so quickly to photons that they cannot produce recoils. So we then estimate the $\nu \rightarrow n$ total cross section according to

$$\sigma_{\text{NIN}} = \sigma_{\text{E}} + \frac{3}{7} \sigma_{\text{RES}}, \quad (8)$$

where we assume that the seven RES processes contribute equally to the RES total cross section. Fixing $E_\nu = 3$ GeV and using the SM prediction for the total neutrino cross section at these energies [37] one then gets $\sigma_{\text{NIN}} = 6.2 \times 10^{-39}$ cm².

With the relevant cross section estimated we can now calculate the expected number of NIN events. Assuming

the full vBDX-DRIFT detector will be made of N_{modules} vBDX-DRIFT modules each having 1 m³ fiducial volumes surrounded by vacuum vessels 150 cm on a side we then write the number of NIN per cycle as follows

$$\frac{N_{\text{NIN}}}{\text{cycle}} = 3.0 \cdot 10^{-4} \left(\frac{\mathcal{F}}{3} \right) \left(\frac{n_{\text{Fe}}}{2.4 \cdot 10^{24}/\text{cm}^3} \right) \left(\frac{n_\nu}{772640/\text{cm}^2} \right) \\ \left(\frac{A}{22500 \text{cm}^2} \right) \left(\frac{t}{1 \text{cm}} \right) \left(\frac{\sigma_{\text{NIN}}}{6.2 \cdot 10^{-39} \text{cm}^2} \right) N_{\text{modules}}. \quad (9)$$

Here \mathcal{F} refers to the number of faces, n_{Fe} to the iron neutron density, n_ν to the number of neutrinos per cycle, A to the area of each face, and t to the vessel wall thickness. We assume only 3 detector faces (front and half of the four lateral faces) are relevant because of forward scattering of the neutrons, while for n_ν we take the on-axis neutrino flux in Fig. 3 rescaled by $n_{\text{POT}}/\text{cycle} = 7.5 \times 10^{13}$ [15]. Taking 1.0 second as a representative LBNF cycle time (LBNF extractions oscillate in the range 0.7-1.2 s [15]), a 10 cubic-meter detector and a data-taking period of 7 years, one gets $N_{\text{NIN}}/7\text{-years} \simeq 6.56 \times 10^5$.

Given the LBNF beamline energy spectrum and the final-state particles in the processes of interest (E and RES), NINs are order GeV. The detection probability \mathcal{P} for those GeV neutrons at vBDX-DRIFT operating with 100% of the fiducial volume filled with CS₂ at 400 Torr has been determined by a GEANT4 [38] simulation benchmarked to neutron-induce nuclear-recoil data [19]. The result is $\mathcal{P} = 2.5 \times 10^{-5}$. With this number we then estimate the number of effective NIN events over the relevant time period and for 10 modules to be

$$\frac{N_{\text{NIN}}^{\text{eff}}}{7\text{-years}} = \mathcal{P} \times \left(\frac{N_{\text{NIN}}}{7\text{-years}} \right) \\ = 16.0. \quad (10)$$

From the CS₂ calculation represented in the left graph of Fig. 4 we expect 367 CEvNS events above threshold for the same exposure. This means that the signal-to-background (NIN) ratio is about 23, a number comparable to what the COHERENT collaboration found for the same type of events (47) [2]. Following this analysis, our conclusion is that the NIN background contamination of the CEvNS signal is small for all possible realistic detector configurations.

NINs produced in the surrounding environment are less concerning as they can be shielded against either passively or actively, e.g. [39].

B. SM and BSM studies with the vBDX-DRIFT detector

Measurements of the CEvNS event spectrum can be used to extract information on the weak mixing angle as well as on the rms radii of neutron distributions. Using COHERENT CsI[Na] and LAr data this approach has been used for $\sin^2 \theta_W$ [40, 41]. It has been used as well in forecasts of near-future reactor-based CEvNS data [42, 43]. These analyses provide relevant information for this SM parameter at renormalization

¹ Coherent pion production, multipion production and kaon production open up as well at these energies, however their total cross sections are smaller [37].

scales of order $\langle q \rangle = \mu \simeq 10^{-2} \text{ GeV}$ and $\mu \simeq 10^{-3} \text{ GeV}$, respectively. An analysis complementary to CEvNS-related experiments has been as well discussed using elastic neutrino-electron scattering with the DUNE near detector [44]. This measurement will provide information at $\mu \simeq 6 \times 10^{-2} \text{ GeV}$, with higher precision than what has been so far obtained by COHERENT and comparable to what will be obtained with e.g. MINER and CONNIE.

Measurements of the rms radii of neutron distributions can be as well performed through the observation of the CEvNS process. From Eq. (1) one can see that information on the CEvNS event spectrum can be translated into limits on $r_{\text{rms}}^n = \sqrt{\langle r_n^2 \rangle}$, encoded in $F_N(q)$. Analyses of these type have been carried out using COHERENT CsI[Na] data in the limit $r_{\text{rms}}^n|_{\text{Cs}} = r_{\text{rms}}^n|_{\text{I}}$, for which Ref. [45] found the 1σ result $r_{\text{rms}}^n|_{\text{Cs,I}} = 5.5_{-1.1}^{+0.9} \text{ fm}$. Later on using the LAr data release a similar analysis found the 90% CL upper limit $r_{\text{rms}}^n < 4.33 \text{ fm}$ [41], a value which mainly applies to ^{40}Ar given its natural abundance. Forecasts of neutron distributions measurements using CEvNS data have been presented in Ref. [46].

In addition to SM measurements, CEvNS can be used as a probe for new physics searches. Using COHERENT data, various BSM scenarios have been studied. They include neutrino non-standard interactions (NSIs) and neutrino generalized interactions, light vector and scalar mediators interactions, sterile neutrinos and neutrino electromagnetic properties (see e.g. [40, 41, 47–55]). To illustrate the capabilities of the vBDX-DRIFT detector and as a proof of principle, here we focus on NSI scenarios. Given the ingoing neutrino flavor the couplings that can be probed are $\varepsilon_{\mu e}$, $\varepsilon_{\mu\mu}$ and $\varepsilon_{\mu\tau}$ (see Section IV B 3 for details). We then focus on these couplings and consider—for simplicity—a single-parameter analysis.

We start our discussion with sensitivities of vBDX-DRIFT to the weak mixing angle and the rms radii of the neutron distributions for carbon, fluorine and lead. We then discuss sensitivities to the neutrino NSI. To determine sensitivities, in all cases we employ a simple single-bin chi-square analysis with the test statistics defined as [2]

$$\chi^2 = \left(\frac{N_{\text{Exp}} - (1 + \alpha)N_{\text{Theo}}(p)}{\sigma} \right)^2 + \left(\frac{\alpha}{\sigma_\alpha} \right)^2, \quad (11)$$

where for N_{Exp} we assume the SM prediction adapted to the case we are interested in (see Sections below), N_{Theo} represents predictions of the underlying hypothesis determined by the values of the parameter(s) p and for the statistical uncertainty we assume $\sigma = \sqrt{N_{\text{Exp}} + B}$. Here B refers to background, which we take to be $B = N_{\text{Exp}} \times f/100$ ($f = 0, 10, 25$). We include as well a systematic uncertainty σ_α along with its nuisance parameter α . In the former we include uncertainties due to the nuclear form factor \mathcal{U}_F and the neutrino flux \mathcal{U}_ν , which we add in quadrature. For both we assume 10%, see Section IV B 2 and Ref. [32].

1. Measurements of the weak mixing angle

Measurements of the weak mixing angle not only provide information on the quantum structure of the SM, but allow

indirectly testing new physics effects at the TeV scale and beyond. The most precise measurements of $\sin^2 \theta_W$ come from: (i) The right-left Z pole production asymmetry measured at SLAC [57], (ii) the $Z \rightarrow b\bar{b}$ forward-backward asymmetry measured at LEP1 [58]. These measurements are known to disagree at the 3.2σ level, so improved experimental determinations are required. Low-energy measurements of $\sin^2 \theta_W$ aim at doing so, with different precisions depending on the experimental techniques employed [56]. Some might be able to reach the level of precision required, some others may not. However, even those not reaching that level (order 0.1%) will be able to test exotic contributions to $\sin^2 \theta_W$ that could be lurking at low energies.

Low-energy measurements of $\sin^2 \theta_W$ at $\langle q \rangle \ll m_Z$ include atomic parity violation in cesium at $\langle q \rangle \simeq 2.4 \text{ MeV}$ [59, 60], electron-electron Møller scattering at $\langle q \rangle \simeq 160 \text{ MeV}$ [61], and ν_μ -nucleus deep-inelastic scattering at $\langle q \rangle \simeq 5 \text{ GeV}$ [62]. More recent measurements involve electron parity-violating deep-inelastic scattering at $\langle q \rangle \simeq 6 \text{ GeV}$ [63] and precision measurements of the weak charge of the proton at $\langle q \rangle \simeq 157 \text{ MeV}$ [64]. The precision of these measurements range from $\pm 0.4\%$ for the weak charge of the proton up to $\pm 4\%$, for electron parity-violating deep-inelastic scattering. Thus, none of them have the level of precision achieved at Z pole measurements, but are precise enough to constraint new physics effects. Future atomic parity violation experiments as well as ultraprecise measurements of parity violation in electron- ^{12}C scattering will improve the determination of $\sin^2 \theta_W$ at the $\sim 0.1\%$ level [56].

As it has been already stressed, CEvNS provides another experimental environment in which information on $\sin^2 \theta_W$ can be obtained. Probably the most ambitious scenario is that of reactor neutrinos: the combination of a large neutrino flux and small baseline provides large statistics with which the weak mixing angle can be determined with a precision of $\pm 0.1\%$ or even below, depending on detector efficiency and systematic errors [43]. For spallation neutron source neutrinos, current precision is of order $\pm 50\%$. However, expectations are that data from future ton-size detectors (LAr and NaI[Tl]) will improve this measurement.

To assess the precision at which vBDX-DRIFT can measure the weak mixing angle we assume two detector configurations in which the bulk of the gas is filled with either carbon disulfide or carbon tetrafluoride. For CS_2 we take the detector pressure to be 411 Torr, while for CF_4 400 Torr. In both cases a 100% detector efficiency is assumed. For N_{exp} we assume the SM prediction calculated with $\sin^2 \theta_W$ extrapolated to low energies [56]:

$$\sin^2 \theta_W(q=0) = \kappa(q=0)_{\overline{\text{MS}}} \sin^2 \theta_W(m_Z)_{\overline{\text{MS}}}, \quad (12)$$

with $\kappa(q=0)_{\overline{\text{MS}}} = 1.03232 \pm 0.00029$ and $\sin^2 \theta_W(m_Z)_{\overline{\text{MS}}} = 0.23122 \pm 0.00003$ [65]. For the calculation we take only central values. With the toy experiment fixed, we then calculate N_{Theo} for $\sin^2 \theta_W \in [0.20, 0.27]$, for which we find that the event yield varies from 280 to 507 events for carbon disulfide and from 589 to 1012 events for carbon tetrafluoride.

The results of the chi-square analysis are shown in Fig. 6, left graph for carbon disulfide and right graph for carbon

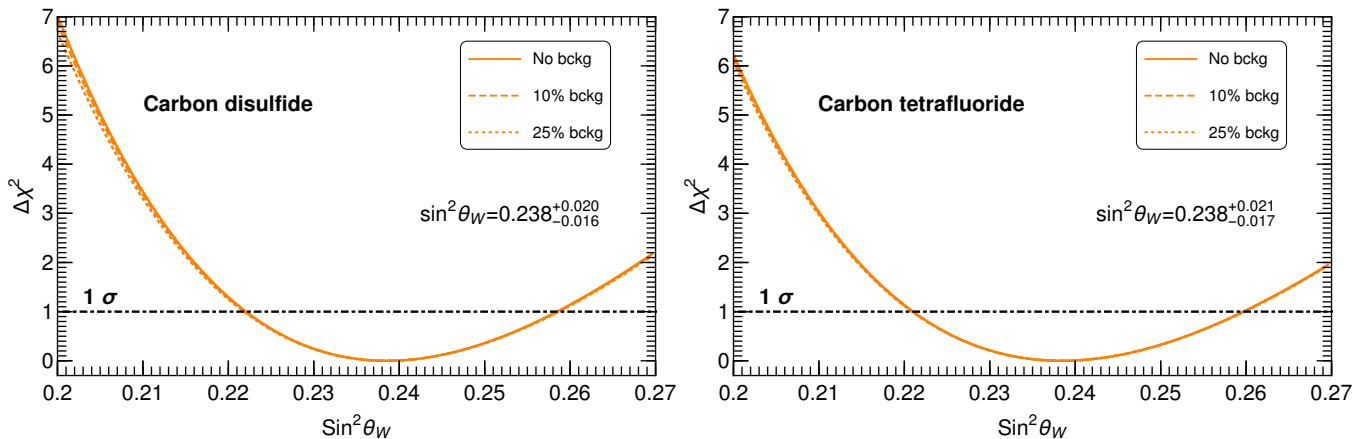


FIG. 6. **Left graph:** Chi-square distribution for $\sin^2 \theta_W$ assuming a ten-cubic meter detector volume, 7-years data taking and 100% detector efficiency. The calculation has been done assuming the bulk of the gas is filled with CS_2 under three background hypotheses: A free background measurement and 10% and 25% of the measured signal, assumed to be the SM prediction at 411 Torr with $\sin^2 \theta_W$ fixed according to its low-energy extrapolation [56]. **Right graph:** Same as left graph but assuming instead that the bulk of the gas is filled with CF_4 at 400 Torr, pressure at which the SM prediction amounts to 808 events/7-years.

tetrafluoride. The level at which $\sin^2 \theta_W$ can be determined depends—of course—on the amount of background, although its impact is not severe. Assuming the detector is operated under zero background conditions we get for both CS_2 and CF_4 the 1σ results:

$$\begin{aligned} \text{CS}_2: \quad \sin^2 \theta_W &= 0.238^{+0.020}_{-0.016}, \\ \text{CF}_4: \quad \sin^2 \theta_W &= 0.238^{+0.021}_{-0.017}. \end{aligned} \quad (13)$$

From these results one can see that the precision with which the weak mixing angle can be measured at vBDX-DRIFT will be of order 8%. That precision exceeds what has been so far achieved with any of the COHERENT detectors, and comparable to what DUNE 7-years data taking could achieve in the electron recoil channel, 3%.

To put in perspective the precision that can be achieved at vBDX-DRIFT, we have plotted the RGE evolution of the weak mixing angle in the $\overline{\text{MS}}$ renormalization scheme along with the low-energy measurements of the high precision experiments we have discussed. We have as well included expectations from the DUNE near detector using elastic neutrino-electron scattering [44]. The result is shown in Fig. 7, left graph. To allow comparison we have reduced the error bar by a factor 2. One can see that although vBDX-DRIFT comes with a larger uncertainty than these high-precision experiments, it brings information at a renormalization scale which is not covered by any of those experiments. We note that the precise location of the scale constrained by the experiment depends on detectors parameters such as the assumed recoil threshold and the shape of the neutrino spectrum. In Fig. 7 we simply plot it at the scale corresponding to the mean recoil energy, which we find agrees within uncertainty with a more rigorous calculation accounting for the shape of the neutrino spectrum. Note that the result we obtain is expected, as it is known that reaching order $\pm 1\%$ precision in neutrino scattering experiments is challeng-

ing [56].

Note that if one focuses on experiments that fall within the same “category” (stopped-pion CEvNS-related experiments) then a more reliable comparison can be done. The right graph in Fig. 7 shows the 1σ sensitivities for COHERENT CsI[Na] and LAr along with what can be achieved at vBDX-DRIFT. We have included as well the $\mu = \langle q \rangle$ range that these experiments cover. For that we have used $q^2 = 2m_N E_r$ along with information on the minimum and maximum recoil energies these experiments have measured, or will in the case of vBDX-DRIFT: COHERENT CsI[Na], $E_r \in [5, 30]$ keV [2]; COHERENT LAr, $E_r \in [19, 81]$ keV [22]; vBDX-DRIFT CS_2 , $E_r \in [101, 2640]$ keV. For the latter we have used $E_\nu^{\text{min}} = 39$ MeV and $E_\nu^{\text{min}} = 200$ MeV, values dictated by the neutrino spectrum low-energy tail and the coherence condition. These values result in

$$\begin{aligned} \text{CsI}: \quad q &\in [35, 86] \times 10^{-3} \text{ GeV}, \\ \text{LAr}: \quad q &\in [38, 78] \times 10^{-3} \text{ GeV}, \\ \text{CS}_2: \quad q &\in [78, 397] \times 10^{-3} \text{ GeV}, \end{aligned} \quad (14)$$

and $\langle q \rangle = 61 \times 10^{-3}$ GeV, $\langle q \rangle = 58 \times 10^{-3}$ GeV and $\langle q \rangle = 238 \times 10^{-3}$ GeV, respectively. One can see that among those stopped-pion CEvNS experiments vBDX-DRIFT has a better performance.

2. Form factor uncertainties and measurements of neutron density distributions

Given the recoil energies involved in the vBDX-DRIFT experiment, one expects the CEvNS event yield to be rather sensitive to nuclear physics effects. Thus to assess the degree at which these effects affect CEvNS predictions, we first calculate the intrinsic uncertainties due to the form factor

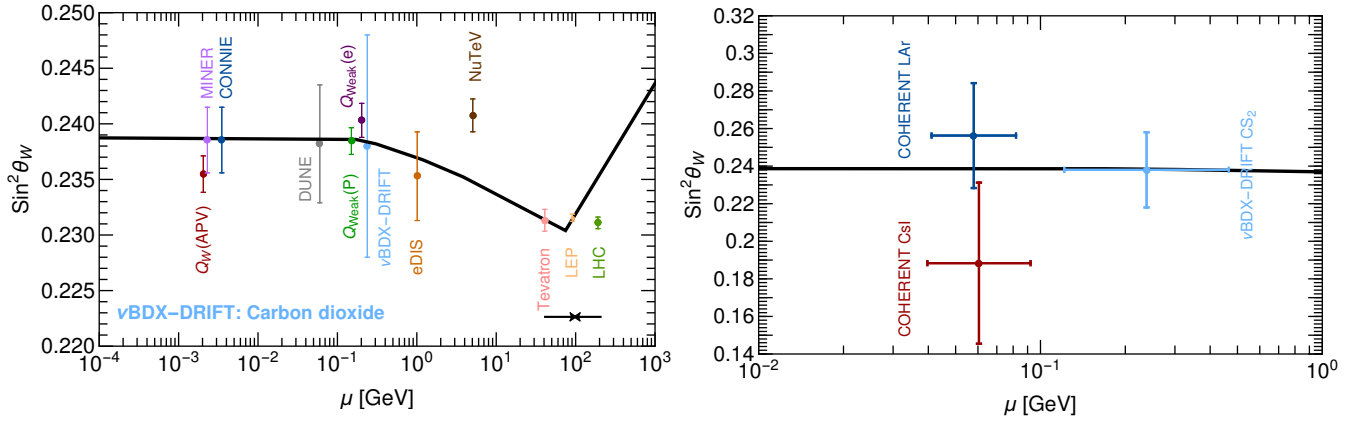


FIG. 7. **Left graph:** Weak mixing angle RGE evolution in the \overline{MS} renormalization scheme as calculated in Ref. [66], along with a variety of measurements at different renormalization scales: Atomic parity violation (APV) [59, 60], MINER [6, 43], CONNIE [8, 43] (slightly offset horizontally for clarity), proton weak charge ($Q_{\text{Weak}}(P)$) from cesium transitions [64], electron weak charge ($Q_{\text{Weak}}(e)$) from Møller scattering [61], parity violation in electron deep inelastic scattering (eDIS) [63], neutrino-nucleus scattering (NuTeV) [62] and collider measurements (Tevatron, LEP and LHC. LEP and LHC results offset horizontally as indicated by the arrows) [65]. Results for the DUNE near detector using elastic neutrino-electron scattering are displayed as well [44]. The result for vBDX-DRIFT follows from the chi-square analysis in the left graph in Fig. 6 and the error bar has been reduced by a factor 2 to allow comparison with the other experiments. **Right graph:** Same as left graph but for fixed-target CEvNS experiments, COHERENT CsI[Na] [2, 40] and LAr [22, 41]. This result shows that measurements at vBDX-DRIFT can be more competitive than those obtained so far with COHERENT data, thus providing complementary information in the nuclear recoil channel to DUNE near detector measurements using the electron channel instead.

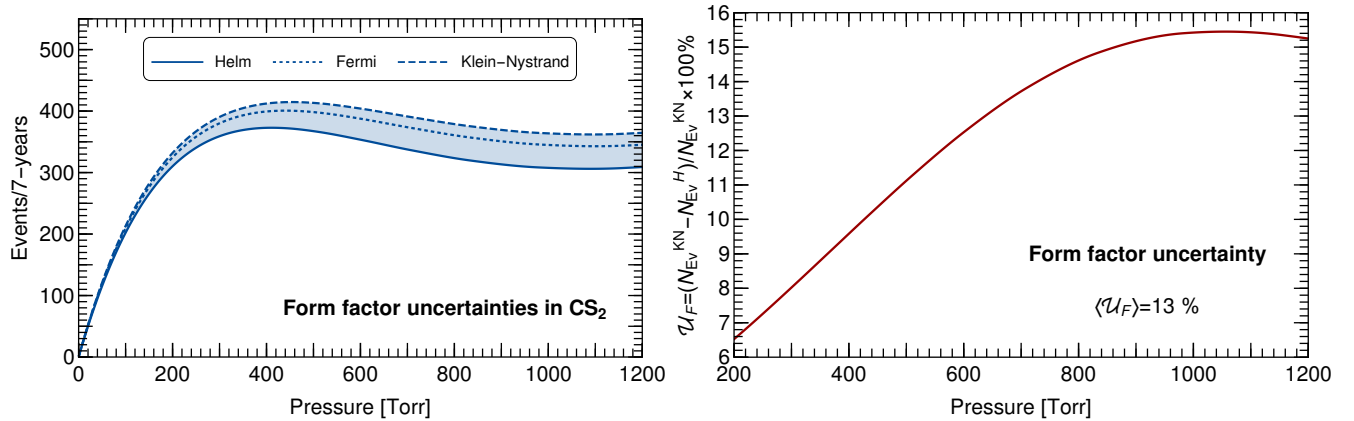


FIG. 8. **Left graph:** CEvNS event yield as a function of pressure for carbon dioxide assuming a ten-cubic meter detector volume and 7-years data taking. The calculation has been done assuming three different form factor parametrizations: Helm form factor, symmetrized Fermi form factor and Klein-Nystrand form factor. The result shows that the smallest (largest) event yield is obtained from the Helm (Klein-Nystrand) form factor. **Right graph:** Percentage uncertainty as a function of pressure calculated from the minimum and maximum event yields. As pressure increases the difference increases as well as a result of increasing neutrino energy.

parametrization choice. For that aim we use—in addition to the Helm form factor parametrization [25]—the Fourier transform of the symmetrized Fermi distribution and the Klein-Nystrand form factor [26, 27].

The Helm model assumes that the proton and neutron distributions are dictated by a convolution of a uniform density of radius R_0 and a Gaussian profile characterized by the folding width s , responsible for the surface thickness. The Helm

form factor then reads [25]

$$F_H(q^2) = 3 \frac{j_1(qR_0)}{qR_0} e^{-(qs)^2/2}, \quad (15)$$

where j_1 is the spherical Bessel function of order one and R_0 , the diffraction radius, is determined by the surface thickness and the rms radius of the corresponding distribution, namely [67]

$$R_0 = \sqrt{\frac{5}{3} (\langle r^2 \rangle_H - 3s^2)}. \quad (16)$$

For the surface thickness we use 0.5 fm [67]. The symmetrized Fermi form factor follows instead from the symmetrized Fermi function, defined through the conventional Fermi or Woods-Saxon function. The resulting form factor is given by [26]

$$F_{\text{SF}}(q^2) = \frac{3}{qc} \left[\frac{\sin(qc)}{(qc)^2} \left(\frac{\pi qa}{\tanh(\pi qa)} - \frac{\cos(qc)}{qc} \right) \right] \frac{\pi qa}{\sinh(\pi qa)} \frac{1}{1 + (\pi a/c)^2}. \quad (17)$$

Here c defines the half-density radius and a the surface diffuseness, both related through the rms radius of the distribution

$$c = \sqrt{\frac{5}{3} \left(\langle r^2 \rangle_{\text{SF}} - \frac{7}{5} (\pi a)^2 \right)}. \quad (18)$$

For the calculation we fix $a = 0.52$ fm [68]. Results are rather insensitive to reasonable changes of this parameter [51]. Finally, the Klein-Nystrand form factor follows from folding a Yukawa potential of range a_k over a hard sphere distribution with radius R_A . The form factor is then given by [27]

$$F_{\text{KN}} = 3 \frac{j_1(qR_A)}{qR_A} \frac{1}{1 + q^2 a_k^2}. \quad (19)$$

In this case the radius R_A and the potential range a_k are related through the rms radius of distribution according to

$$R_A = \sqrt{\frac{5}{3} (\langle r^2 \rangle_{\text{KN}} - 6a_k^2)}, \quad (20)$$

with the value for a_k given by 0.7 fm [27].

With these results at hand we are now in a position to calculate the CEvNS event yield. We do so for carbon disulfide assuming the detector specifications used in our previous analyses. The result is displayed in Fig. 8 left graph, from which it can be seen that the event yield has a relative mild dependence on the nuclear form factor choice. The minimum and maximum values interpolate between the results obtained using the Helm and Klein-Nystrand form factors. It is worth noting that for reactor neutrinos, form factor effects are completely negligible while for SNS neutrinos (COHERENT) they are mild, of order 5% or so [2]. In this case the dependence is stronger, a result expected given the energy regime of the neutrino probe. Right graph in Fig. 8 shows the percentage uncertainty calculated according to

$$\mathcal{U}_F = \frac{N_{\text{ev}}^{\text{KN}} - N_{\text{ev}}^{\text{H}}}{N_{\text{ev}}^{\text{KN}}} \times 100\%, \quad (21)$$

and covering pressures up to 1200 Torr. From this result it can be seen that at low recoil energy thresholds uncertainties are of order 6–7%, and raise up to order 16% at high recoil energy thresholds. Calculation of the average uncertainty results in $\langle \mathcal{U}_F \rangle \simeq 13\%$. This means that calculation of SM CEvNS predictions as well as possible new physics effects always come along with such uncertainty. Note that our calculations in the

previous Sections, based on the Helm form factor, should be understood as lower limit predictions of what should be expected.

We now turn to the discussion of measurements of neutron distributions, in particular, of the rms radius of the neutron distribution. This quantity is relevant since, combined with the rms radius of the proton distribution, it defines the neutron skin thickness of a nucleus, $\Delta r_{np}(\text{nucleus}) = r_{\text{rms}}^n - r_{\text{rms}}^p$. This quantity in turn is relevant in nuclear physics as well as in astrophysics. For instance, in nuclear physics it plays an important role in the nuclear energy density functional [69–73], while in astrophysics it allows the prediction of neutron star properties such as its density and radius [74].

A clean direct measurement of the neutron rms radius has been done only for ^{208}Pb by the PREX experiment at the Jefferson laboratory [75, 76]. The rms radii for other nuclides have been mapped using hadronic experiments, and suffer from large uncontrolled uncertainties [77]. In contrast to these experiments, PREX relies on parity-violating elastic electron scattering thus providing a clean determination not only of the neutron rms radius but of the neutron skin of ^{208}Pb . As we have already mentioned, CEvNS experiments provide an alternative experimental avenue to determine this quantity for other nuclides.

To prove the capabilities of the vBDX-DRIFT detector we calculate sensitivities for carbon, fluorine and lead. Measurements of the rms radius of the neutron distribution for carbon and fluorine can be done using CF_4 . Since carbon and fluorine have about the same amount of neutrons, in first approximation one can assume $r_{\text{rms}}^n|_{\text{C}} = r_{\text{rms}}^n|_{\text{F}} = r_{\text{rms}}^n$. The analysis for lead can be done using instead $\text{C}_8\text{H}_{20}\text{Pb}$. In this case the large mismatch between the number of neutrons for carbon and lead does not allow the approximation employed for CF_4 . Experimentally, however, that measurement could be carried out by tuning pressure to the value at which the lead signal peaks (6.4 Torr) and then selecting lead events. The latter enabled by the different ranges for carbon and lead given an ionization. Following this strategy we then calculate $r_{\text{rms}}^n|_{\text{Pb}}$ using only the lead signal. Note that this analysis intrinsically assumes that all lead stable nuclei (^{204}Pb , ^{206}Pb , ^{207}Pb and ^{208}Pb) have the same r_{rms}^n . This of course is not the case, but it is a rather reasonable assumption given the precision at which the r_{rms}^n can be measured at vBDX-DRIFT.

To determine sensitivities we use as toy experiment input the SM prediction assuming $r_{\text{rms}}^n = \langle r_{\text{rms}}^p \rangle$, where $\langle r_{\text{rms}}^p \rangle$ is calculated according to $\sum_i r_{\text{rms},i}^p X_i$ with $r_{\text{rms},i}^p$ the proton rms radius of i^{th} stable isotope [30] and X_i its natural abundance. We then perform our statistical analysis by calculating the event yield by varying r_{rms}^n within [2.3, 3.3] fm for CF_4 and [4.2, 6.4] fm for $\text{C}_8\text{H}_{20}\text{Pb}$. Results are shown in Fig. 9. Top-left and bottom-left graphs show the variation of the event rate in terms of r_{rms}^n for CF_4 and $\text{C}_8\text{H}_{20}\text{Pb}$ respectively. One can see that the signal increases with decreasing r_{rms}^n , a behavior that can be readily understood from the reduction in nuclear size implied by a smaller r_{rms}^n : As nuclear size reduces, coherence extends to larger transferred momentum.

Results of the chi-square analyses are shown in the top-right and bottom-right graphs. In each case results for our three

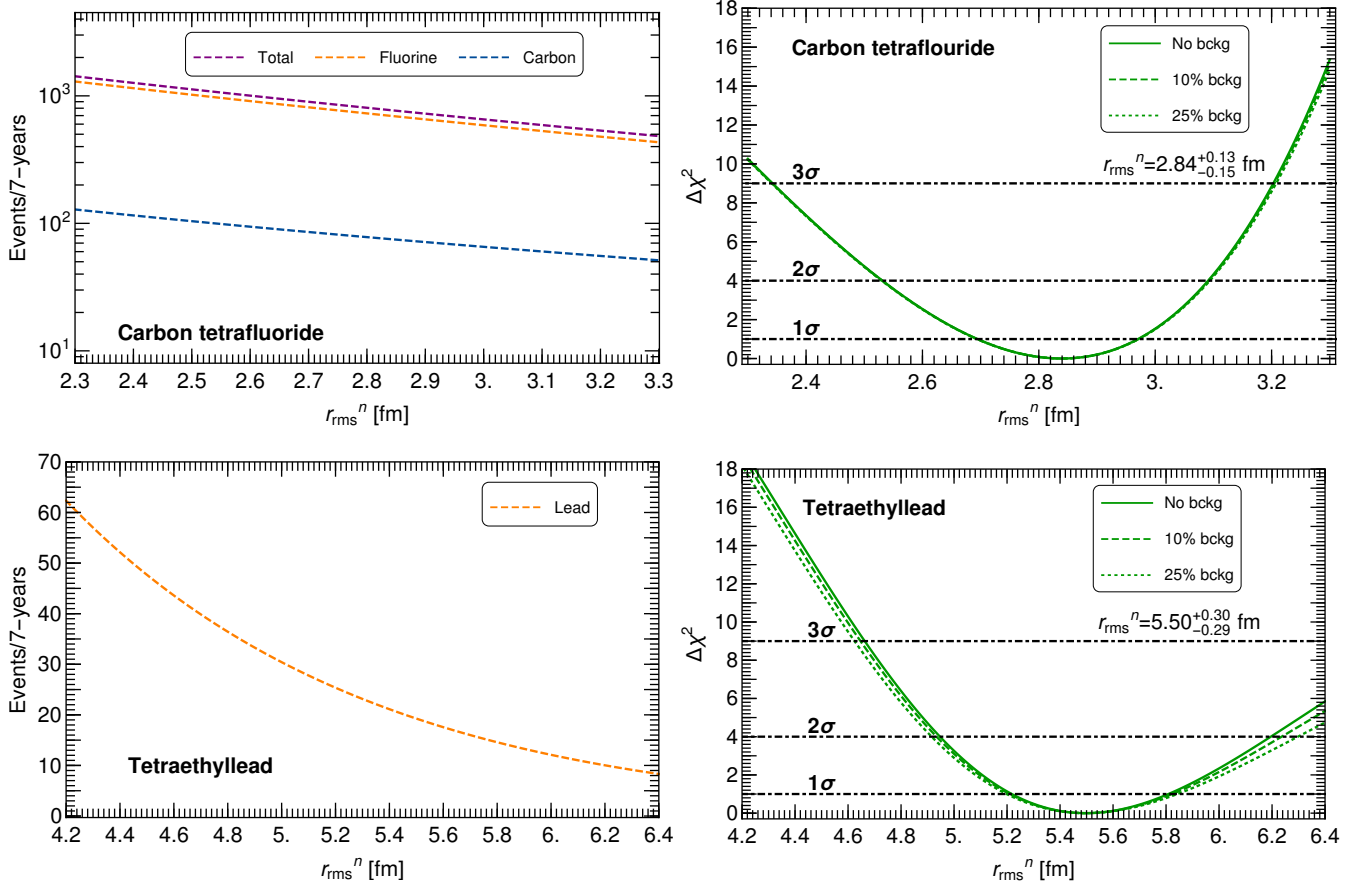


FIG. 9. **Top-left graph:** Event distribution in terms of the neutron rms radius for CF_4 . **Top-right graph:** Chi-square distribution for the neutron rms radii of carbon and fluorine including our three background hypotheses. For the calculation we have assumed a ten-cubic meter detector volume, 7-years data taking and 100% detector efficiency. The value for the neutron rms radius follows from the background-free case, a potential experimental scenario given the directional properties of the vBDX-DRIFT detector. We assume 100% of the detector is filled with CF_4 . **Bottom-left graph:** Event distribution in terms of the neutron rms radius for $\text{C}_8\text{H}_{20}\text{Pb}$. **Bottom-right graph:** Chi-square distribution for the neutron rms radius of lead under the assumptions used in the carbon and fluorine case. A 2.3:1 ($\text{CS}_2 : \text{C}_8\text{H}_{20}\text{Pb}$) gas ratio has been assumed. The chi-square analyses include systematics due to form factor parametrization dependences as well as neutrino flux uncertainties.

background hypotheses are displayed. These results demonstrate that the ten-cubic meter and 7-years data taking vBDX-DRIFT will be able to set the following 1σ measurements:

$$\begin{aligned} \text{C and F in } \text{CF}_4 : r_{\text{rms}}^n &= 2.84_{-0.15}^{+0.13} \text{ fm} , \\ \text{Pb in } \text{C}_8\text{H}_{20}\text{Pb} : r_{\text{rms}}^n &= 5.50_{-0.29}^{+0.30} \text{ fm} . \end{aligned} \quad (22)$$

From these numbers one can see that the neutron rms radius for carbon and fluorine can be determined at the 3% accuracy level, while for lead at about 5%. The difference in precision has to do with the difference in statistics. For CF_4 about 800 events are available, while for lead in $\text{C}_8\text{H}_{20}\text{Pb}$ only about 19 due to the constraints implied by the differentiation between lead and carbon events. Note that these measurements will not only provide information on these quantities, but can potentially be used to improve attempts to reliably extract neutron star radii, in particular those for lead.

3. Sensitivities to neutrino NSI

Neutrino NSI are four-fermion contact interactions which parametrize a new vector force relative to the electroweak interaction in terms of a set of twelve flavored-dependent new parameters (in the absence of CP-violating phases). Explicitly they read [79]

$$\mathcal{L}_{\text{NSI}} = -\sqrt{2}G_F \sum_{q=u,d} \bar{\nu}_a \gamma_\mu (1 - \gamma_5) \nu_b \bar{q} \gamma^\mu \left(\epsilon_{ab}^{Vq} + \epsilon_{ab}^{Aq} \gamma_5 \right) q , \quad (23)$$

where a, b, \dots are lepton flavor indices. The axial current parameters generate spin-dependent interactions and hence are poorly constrained. For that reason most NSI analyses consider only vector couplings $\epsilon_{ab}^q \equiv \epsilon_{ab}^{Vq}$. Limits on NSI are abundant and follow from a variety of measurements which include neutrino oscillations experiments [80, 81], low energy scattering processes [82] and LHC data [83, 84]. In the light of COHERENT CEvNS data they have been extensively con-

| vBDX-DRIFT CS ₂ (7-years) | | COHERENT CsI (1-year) | |
|--------------------------------------|---------------------------------------|-----------------------|-------------------------------------|
| $\epsilon_{\mu\mu}^u$ | $[-0.013, 0.011] \oplus [0.30, 0.32]$ | $\epsilon_{\mu\mu}^u$ | $[-0.06, 0.03] \oplus [0.37, 0.44]$ |
| $\epsilon_{e\mu}^u$ | $[-0.064, 0.064]$ | $\epsilon_{e\mu}^u$ | $[-0.13, 0.13]$ |

TABLE I. 1σ allowed ranges for neutrino NSI couplings derived from a single-parameter analysis. Results for down quark parameters are rather close to those derived for up quarks, so are not displayed. Intervals for $\epsilon_{\mu\tau}^q$ ($q = u, d$) are identical to those for $\epsilon_{e\mu}^q$. For 1-year data taking sensitivities can be degraded by up to a factor 5. Allowed 1σ limits from COHERENT CsI including spectra and timing information are taken from Ref. [78], are shown for comparison.

sidered as well [40, 41, 47, 78, 85], and their potential experimental traces have been the subject of studies in multi-ton DM experiments [86–89].

The presence of neutrino NSI modify the CEvNS differential cross section. Being vector interactions the flavor-diagonal couplings interfere with the SM contribution, that interference can be constructive or destructive depending on the sign the coupling comes along with. In contrast, off-diagonal couplings always enhance the SM cross section. Assuming equal rms radii for the proton and neutron distributions, the modified cross section proceeds from Eq. (1) by changing the coherent weak charge according to [90]

$$Q_{Wa}^2 = \left[Z(g_V^p + 2\epsilon_{aa} + \epsilon_{aa}^d) + (A - Z)(g_V^n + \epsilon_{aa} + \epsilon_{aa}^d) \right]^2 + \sum_{a \neq b} \left[Z(2\epsilon_{ab}^u + \epsilon_{ab}^d) + (A - Z)(\epsilon_{ab}^u + 2\epsilon_{ab}^d) \right]^2. \quad (24)$$

The new parameter dependence can lead to flavor-dependent cross sections. An incoming flavor state ν_a can produce either the same flavor state or an orthogonal one ν_b . The first term in Eq. (24) accounts for $\nu_a \rightarrow \nu_a$ scattering, while the second to scattering to a flavor orthogonal state. Using the LBNF beamline, three NSI couplings—per first generation quarks—can therefore be tested: $\epsilon_{\mu\mu}^q$, $\epsilon_{e\mu}^q$ and $\epsilon_{\mu\tau}^q$.

Calculation of sensitivities is done assuming one parameter at a time. A procedure that is justified by the fact that is for this parameter configurations for which the best sensitivities can be derived. In all cases we vary the effective parameter in the interval $[-1.0, 1.0]$. The results of the analysis are shown in Fig. 10. Left graph for $\epsilon_{\mu\mu}^u$ and right graph for $\epsilon_{e\mu}^u$ (results for down quark couplings follow closely those for up quark parameters, so are not shown). Note that due to the adopted single-parameter analysis results for $\epsilon_{\mu\tau}^u$ are identical to those from $\epsilon_{e\mu}^u$. Table I summarizes the 1σ sensitivities that can be achieved along with 1σ intervals derived using COHERENT CsI spectral and timing information [78].

For the flavor-diagonal coupling we find two disconnected allowed regions, a result which is expected. The region around zero—which includes the SM solution $\epsilon_{\mu\mu}^u = 0$ —is open just because contributions from the NSI parameter generate small deviations from the SM prediction. The region of large NSI—which does not include the SM solution—is viable because the NSI and SM contributions destructively interfere, with the NSI contribution exceeding in about a factor 2 the SM terms resulting in $-|Q_W| \rightarrow Q_W$. For the off-diagonal coupling results are as well as expected. Since it contributes construc-

tively enhancing the SM prediction, the chi-square distribution is symmetric around $\epsilon_{\mu\mu}^u = 0$. Compared with results derived using COHERENT CsI spectral and timing information, one can see that in all cases sensitivities improve. For $\epsilon_{\mu\mu}^u$ sensitivities are better by about a factor 3 (left interval) and 1.3 (right interval). For $\epsilon_{e\mu}^u$ they improve by about a factor 2. These numbers apply as well to the other NSI parameters not displayed. All in all one can see that vBDX-DRIFT data will allow test region of NSI parameters not yet covered by COHERENT measurements.

V. CONCLUSIONS

In this paper a new idea to study CEvNS with the vBDX-DRIFT detector has been considered. We have quantified sensitivities to the weak mixing angle using carbon disulfide as target material. Our findings demonstrate that a determination of this parameter at a renormalization scale within $\sim [0.1, 0.4]$ GeV can be done at the 8% level, thus providing complementary information to future measurements at DUNE using the electron recoil channel. We have investigated as well sensitivities to the neutron distributions of carbon, fluorine and lead using carbon tetrafluoride and tetraethyllead as target materials. Our results show that measurements with accuracies of order 5% and 10%, respectively, can be achieved. Finally, we have assessed sensitivities to new physics searches and for that aim we have considered effective neutrino NSI. Given the incoming neutrino flavor, at vBDX-DRIFT only muon-flavor NSI parameters can be tested. Using carbon disulfide as target material, flavor-diagonal (off-diagonal) couplings of order 10^{-3} (10^{-2}) can be proven. In the absence of a signal these numbers will translate in significant improvements of current limits.

Due to its directional and background rejection capabilities, the vBDX-DRIFT detector combined with the LBNF beamline provides a unique opportunity to study CEvNS in a neutrino energy range not yet explored. We estimated the ratio of the most important beam related neutrino-induced neutron background to the CEvNS signal to be small, about a factor 23 smaller. The detector offers a rich neutrino physics program—along with a potential agenda for light DM searches—that includes measurements of the CEvNS cross section in nuclides not used by other technologies, measurements of the weak mixing angle in an energy regime not yet explored by any other neutrino scattering experiment, measurements of neutron distributions as well as searches for new physics in the

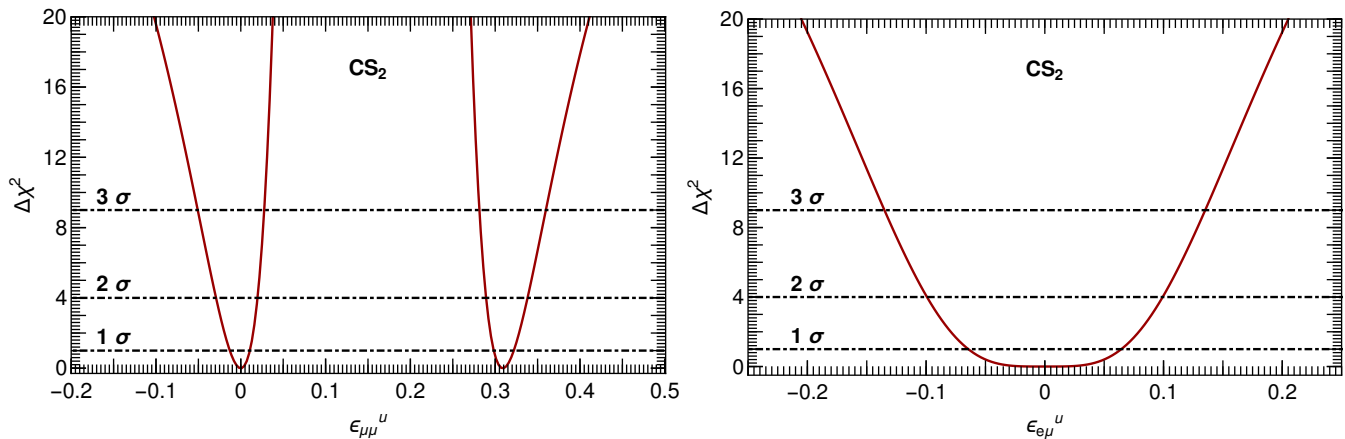


FIG. 10. **Left graph:** Chi-Square distribution for $\epsilon_{\mu\mu}^u$ assuming the background-free hypothesis. Deviations due to background (10% and 25% of the signal rate) are small. For the calculation we have assumed 100% of the ten-cubic meter detector volume is filled with CS_2 and 7-years of data taking. **Right graph:** Same as left graph but for the off-diagonal coupling $\epsilon_{e\mu}^u$ (or $\epsilon_{\mu\tau}^u$). Results for down quark parameters are rather close to those found in this case and so are not displayed.

neutrino sector.

ACKNOWLEDGMENTS

We thank Dinesh Loomba for discussions since the early stages of this work as well as for his suggestions on the

manuscript. We thank Phil Barbeau, Pedro Machado and Kate Scholberg for comments on the manuscript. DAS is supported by the grant “Unraveling new physics in the high-intensity and high-energy frontiers”, Fondecyt No 1171136. BD and LES acknowledge support from DOE Grant de-sc0010813. The work of DK is supported by DOE under Grant No. DE-FG02-13ER41976/ DE-SC0009913/DE-SC0010813.

-
- [1] D. Z. Freedman, *Phys. Rev.* **D9**, 1389 (1974).
[2] D. Akimov et al. (COHERENT), *Science* (2017), 1708.01294.
[3] D. Akimov et al. (COHERENT), *Phys. Rev. Lett.* **126**, 012002 (2021), 2003.10630.
[4] H. T. Wong et al. (TEXONO), *Phys. Rev. D* **75**, 012001 (2007), hep-ex/0605006.
[5] J. Billard et al., *J. Phys. G* **44**, 105101 (2017), 1612.09035.
[6] G. Agnolet et al. (MINER), *Nucl. Instrum. Meth. A* **853**, 53 (2017), 1609.02066.
[7] Y. J. Ko et al. (NEOS), *Phys. Rev. Lett.* **118**, 121802 (2017), 1610.05134.
[8] A. Aguilar-Arevalo et al. (CONNIE), *Phys. Rev. D* **100**, 092005 (2019), 1906.02200.
[9] G. Angloher et al. (NUCLEUS), *Eur. Phys. J. C* **79**, 1018 (2019), 1905.10258.
[10] D. Y. Akimov et al. (RED-100), *JINST* **15**, P02020 (2020), 1910.06190.
[11] G. Fernandez-Moroni, P. A. Machado, I. Martinez-Soler, Y. F. Perez-Gonzalez, D. Rodrigues, and S. Rosauro-Alcaraz (2020), 2009.10741.
[12] D. Akimov et al. (COHERENT) (2018), 1803.09183.
[13] D. Baxter et al., *JHEP* **02**, 123 (2020), 1911.00762.
[14] C. Bellenghi, D. Chiesa, L. Di Noto, M. Pallavicini, E. Previtali, and M. Vignati, *Eur. Phys. J. C* **79**, 727 (2019), 1905.10611.
[15] J. Strait et al. (DUNE) (2016), 1601.05823.
[16] M. Abdullah, D. Aristizabal Sierra, B. Dutta, and L. E. Strigari, *Phys. Rev. D* **102**, 015009 (2020), 2003.11510.
[17] D. P. Snowden-Ifft, J. L. Harton, N. Ma, and F. G. Schuckman, *Phys. Rev.* **D99**, 061301 (2019), 1809.06809.
[18] D. P. Snowden-Ifft and J. L. Gauvreau, *Rev. Sci. Instrum.* **84**, 053304 (2013), 1301.7145.
[19] J. B. R. Battat, A. C. Ezeribe, J. L. Gauvreau, J. L. Harton, R. Lafler, E. Law, E. R. Lee, D. Loomba, A. Lumnah, E. H. Miller, et al. (DRIFT), *Astropart. Phys.* **91**, 65 (2017), 1701.00171.
[20] D. P. Snowden-Ifft, *Rev. Sci. Instrum.* **85**, 013303 (2014).
[21] J. B. R. Battat, J. Brack, E. Daw, A. Dorofeev, A. C. Ezeribe, J. L. Gauvreau, M. Gold, J. L. Harton, J. M. Landers, E. Law, et al. (DRIFT), *Phys. Dark Univ.* **9-10**, 1 (2015), 1410.7821.
[22] D. Akimov et al. (COHERENT) (2020), 2006.12659.
[23] R. Strauss et al., *Eur. Phys. J. C* **77**, 506 (2017), 1704.04320.
[24] D. Z. Freedman, D. N. Schramm, and D. L. Tubbs, *Ann. Rev. Nucl. Part. Sci.* **27**, 167 (1977).
[25] R. H. Helm, *Phys. Rev.* **104**, 1466 (1956).
[26] D. W. L. Sprung and J. Martorell, *Journal of Physics A: Mathematical and General* **30**, 6525 (1997), URL <http://stacks.iop.org/0305-4470/30/i=18/a=026>.
[27] S. Klein and J. Nystrand, *Phys. Rev.* **C60**, 014903 (1999), hep-ph/9902259.
[28] D. Aristizabal Sierra, J. Liao, and D. Marfatia, *JHEP* **06**, 141 (2019), 1902.07398.
[29] M. Hoferichter, J. Menéndez, and A. Schwenk, *Phys. Rev. D* **102**, 074018 (2020), 2007.08529.
[30] I. Angeli and K. P. Marinova, *Atom. Data Nucl. Data Tabl.* **99**, 69 (2013).

- [31] S. Burgos et al., *Astropart. Phys.* **28**, 409 (2007), 0707.1488.
- [32] B. Abi et al. (DUNE) (2020), 2002.03005.
- [33] D. Aristizabal Sierra, B. Dutta, D. Kim, D. Loomba, D. Snowden-Ifft, and L. Strigari, *Work in progress* (2021).
- [34] D. Snowden-Ifft, *Work in progress* (2021).
- [35] D. Snowden-Ifft, *Work in progress* (2021).
- [36] E. Kolbe and K. Langanke, *Phys. Rev. C* **63**, 025802 (2001), nucl-th/0003060.
- [37] J. A. Formaggio and G. P. Zeller, *Rev. Mod. Phys.* **84**, 1307 (2012), 1305.7513.
- [38] S. Agostinelli et al. (GEANT4), *Nucl. Instrum. Meth.* **A506**, 250 (2003).
- [39] S. Westerdale, E. Shields, and F. Calaprice, *Astropart. Phys.* **79**, 10 (2016).
- [40] D. K. Papoulias and T. S. Kosmas, *Phys. Rev.* **D97**, 033003 (2018), 1711.09773.
- [41] O. Miranda, D. Papoulias, G. Sanchez Garcia, O. Sanders, M. Tórtola, and J. Valle, *JHEP* **05**, 130 (2020), 2003.12050.
- [42] B. Canas, E. Garces, O. Miranda, M. Tortola, and J. Valle, *Phys. Lett. B* **761**, 450 (2016), 1608.02671.
- [43] B. Cañas, E. Garcés, O. Miranda, and A. Parada, *Phys. Lett. B* **784**, 159 (2018), 1806.01310.
- [44] A. de Gouvea, P. A. Machado, Y. F. Perez-Gonzalez, and Z. Tabrizi, *Phys. Rev. Lett.* **125**, 051803 (2020), 1912.06658.
- [45] M. Cadeddu, C. Giunti, Y. F. Li, and Y. Y. Zhang, *Phys. Rev. Lett.* **120**, 072501 (2018), 1710.02730.
- [46] P. Coloma, I. Esteban, M. C. Gonzalez-Garcia, and J. Menendez, *JHEP* **08**, 030 (2020), 2006.08624.
- [47] J. Liao and D. Marfatia, *Phys. Lett.* **B775**, 54 (2017), 1708.04255.
- [48] P. Coloma, M. C. Gonzalez-Garcia, M. Maltoni, and T. Schwetz (2017), 1708.02899.
- [49] P. Coloma, I. Esteban, M. C. Gonzalez-Garcia, and M. Maltoni, *JHEP* **02**, 023 (2020), [Addendum: *JHEP* **12**, 071 (2020)], 1911.09109.
- [50] Y. Farzan, M. Lindner, W. Rodejohann, and X.-J. Xu, *JHEP* **05**, 066 (2018), 1802.05171.
- [51] D. Aristizabal Sierra, V. De Romeri, and N. Rojas, *JHEP* **09**, 069 (2019), 1906.01156.
- [52] D. Aristizabal Sierra, V. De Romeri, and N. Rojas, *Phys. Rev.* **D98**, 075018 (2018), 1806.07424.
- [53] O. G. Miranda, D. K. Papoulias, M. Tórtola, and J. W. F. Valle, *JHEP* **07**, 103 (2019), 1905.03750.
- [54] D. K. Papoulias, *Phys. Rev. D* **102**, 113004 (2020), 1907.11644.
- [55] B. Dutta, S. Liao, S. Sinha, and L. E. Strigari, *Phys. Rev. Lett.* **123**, 061801 (2019), 1903.10666.
- [56] K. Kumar, S. Mantry, W. Marciano, and P. Souder, *Ann. Rev. Nucl. Part. Sci.* **63**, 237 (2013), 1302.6263.
- [57] K. Abe et al. (SLD), *Phys. Rev. Lett.* **84**, 5945 (2000), hep-ex/0004026.
- [58] ALEPH and CDF and D0 and DELPHI and L3 and OPAL and SLD and LEP Electroweak Working Group and Tevatron Electroweak Working Group and SLD Electroweak and Heavy Flavour Groups (2010), 1012.2367.
- [59] C. Wood, S. Bennett, D. Cho, B. Masterson, J. Roberts, C. Tanner, and C. E. Wieman, *Science* **275**, 1759 (1997).
- [60] V. Dzuba, J. Berengut, V. Flambaum, and B. Roberts, *Phys. Rev. Lett.* **109**, 203003 (2012), 1207.5864.
- [61] P. Anthony et al. (SLAC E158), *Phys. Rev. Lett.* **95**, 081601 (2005), hep-ex/0504049.
- [62] G. P. Zeller et al. (NuTeV), *Phys. Rev. Lett.* **88**, 091802 (2002), [Erratum: *Phys. Rev. Lett.* **90**, 239902(2003)], hep-ex/0110059.
- [63] D. Wang et al. (PVDIS), *Nature* **506**, 67 (2014).
- [64] D. Androić et al. (Qweak), *Nature* **557**, 207 (2018), 1905.08283.
- [65] M. Tanabashi et al. (Particle Data Group), *Phys. Rev. D* **98**, 030001 (2018).
- [66] J. Erler and M. J. Ramsey-Musolf, *Phys. Rev. D* **72**, 073003 (2005), hep-ph/0409169.
- [67] J. D. Lewin and P. F. Smith, *Astropart. Phys.* **6**, 87 (1996).
- [68] J. Piekarewicz, A. R. Linero, P. Giuliani, and E. Chicken, *Phys. Rev.* **C94**, 034316 (2016), 1604.07799.
- [69] P.-G. Reinhard and W. Nazarewicz, *Phys. Rev. C* **81**, 051303 (2010), 1002.4140.
- [70] P.-G. Reinhard, J. Piekarewicz, W. Nazarewicz, B. Agrawal, N. Paar, and X. Roca-Maza, *Phys. Rev. C* **88**, 034325 (2013), 1308.1659.
- [71] W. Nazarewicz, P.-G. Reinhard, W. Satula, and D. Vretenar, *Eur. Phys. J. A* **50**, 20 (2014), 1307.5782.
- [72] W.-C. Chen and J. Piekarewicz, *Phys. Lett. B* **748**, 284 (2015), 1412.7870.
- [73] W.-C. Chen and J. Piekarewicz, *Phys. Rev. C* **90**, 044305 (2014), 1408.4159.
- [74] C. Horowitz and J. Piekarewicz, *Phys. Rev. Lett.* **86**, 5647 (2001), astro-ph/0010227.
- [75] S. Abrahamyan et al., *Phys. Rev. Lett.* **108**, 112502 (2012), 1201.2568.
- [76] C. Horowitz, K. Kumar, and R. Michaels, *Eur. Phys. J. A* **50**, 48 (2014), 1307.3572.
- [77] C. Horowitz, E. Brown, Y. Kim, W. Lynch, R. Michaels, A. Ono, J. Piekarewicz, M. Tsang, and H. Wolter, *J. Phys. G* **41**, 093001 (2014), 1401.5839.
- [78] C. Giunti, *Phys. Rev. D* **101**, 035039 (2020), 1909.00466.
- [79] L. Wolfenstein, *Phys. Rev.* **D17**, 2369 (1978).
- [80] F. J. Escrihuela, M. Tortola, J. W. F. Valle, and O. G. Miranda, *Phys. Rev. D* **83**, 093002 (2011), 1103.1366.
- [81] M. C. Gonzalez-Garcia, M. Maltoni, and T. Schwetz, *Nucl. Phys.* **B908**, 199 (2016), 1512.06856.
- [82] P. Coloma, P. B. Denton, M. C. Gonzalez-Garcia, M. Maltoni, and T. Schwetz, *JHEP* **04**, 116 (2017), 1701.04828.
- [83] A. Friedland, M. L. Graesser, I. M. Shoemaker, and L. Vecchi, *Phys. Lett. B* **714**, 267 (2012), 1111.5331.
- [84] D. Buarque Franzosi, M. T. Frandsen, and I. M. Shoemaker, *Phys. Rev.* **D93**, 095001 (2016), 1507.07574.
- [85] B. Dutta, R. F. Lang, S. Liao, S. Sinha, L. Strigari, and A. Thompson, *JHEP* **20**, 106 (2020), 2002.03066.
- [86] B. Dutta, S. Liao, L. E. Strigari, and J. W. Walker, *Phys. Lett.* **B773**, 242 (2017), 1705.00661.
- [87] D. Aristizabal Sierra, N. Rojas, and M. H. G. Tytgat, *JHEP* **03**, 197 (2018), 1712.09667.
- [88] M. C. Gonzalez-Garcia, M. Maltoni, Y. F. Perez-Gonzalez, and R. Zukanovich Funchal, *JHEP* **07**, 019 (2018), 1803.03650.
- [89] D. Aristizabal Sierra, B. Dutta, S. Liao, and L. E. Strigari, *JHEP* **12**, 124 (2019), 1910.12437.
- [90] J. Barranco, O. G. Miranda, and T. I. Rashba, *JHEP* **12**, 021 (2005), hep-ph/0508299.